ACADEMIC PRESS

Available online at www.sciencedirect.com

SCIENCE DIRECT®

Journal of Magnetic Resonance 162 (2003) 113–121

JMR Journal of Magnetic Resonance

www.elsevier.com/locate/jmr

Artifacts in $T_{1\rho}$-weighted imaging: correction with a self-compensating spin-locking pulse

Sridhar R. Charagundla,* Arijitt Borthakur, John S. Leigh, and Ravinder Reddy

B1 Stellar-Chance Laboratories, MMRRCC, Department of Radiology, University of Pennsylvania, 422 Curie Boulevard, Philadelphia, PA 19104-6100, USA

Received 11 July 2002; revised 2 December 2002

Abstract

Significant artifacts arise in $T_{1\rho}$-weighted imaging when nutation angles suffer small deviations from their expected values. These artifacts vary with spin-locking time and amplitude, severely limiting attempts to perform quantitative imaging or measurement of $T_{1\rho}$ relaxation times. A theoretical model explaining the origin of these artifacts is presented in the context of a $T_{1\rho}$-prepared fast spin-echo imaging sequence. Experimentally obtained artifacts are compared to those predicted by theory and related to B_1 inhomogeneity. Finally, a ''self-compensating'' spin-locking preparatory pulse cluster is presented, in which the second half of the spin-locking pulse is phase-shifted by 180°. Use of this pulse sequence maintains relatively uniform signal intensity despite large variations in flip angle, greatly reducing artifacts in $T_{1\rho}$-weighted imaging.

Keywords: $T_{1\rho}$; MRI; Artifacts; B_1; Rotary echo

1. Introduction

$T_{1\rho}$, the spin–lattice relaxation time in the rotating frame, represents the time constant of transverse magnetization decay that occurs during the application of a ''spin-locking'' pulse, of amplitude B_{sl}, aligned with the net magnetization vector. Tissue characterization using $T_{1\rho}$ imaging is currently under investigation for multiple tissue types and organ systems, including head and neck neoplasms, cartilage, muscle, and brain [1–9]. The length of time for which the spin-locking pulse is applied varies, depending on the T_2 of the tissue of interest, but is often on the order of 50–100 ms.

If the magnetization vector is poorly aligned with the spin-locking pulse, there is ample opportunity for it to undergo pronounced off-axis nutation, resulting in an unexpected orientation at the end of spin-locking. This occurs in the case of an inhomogeneous B_1, where nutation angles are spatially varying, and in our experience, this may result in dramatically non-uniform image artifacts that markedly degrade any attempts at quantitative imaging. This is a particular hindrance to such applications as $H_2{}^{17}O$ imaging, where sensitivity to small changes in signal intensity is critical; artifacts can easily obscure these small changes in experimental images [10–12]. Furthermore, the artifacts themselves are dependent on spin-locking time and B_{sl}, which precludes accurate measurement of $T_{1\rho}$ and $T_{1\rho}$ dispersion.

Here, we present a theoretical and experimental analysis of artifacts in $T_{1\rho}$ imaging in phantoms and establish their relationship to B_1 inhomogeneity. Dependence of these artifacts on spin-locking time and B_1 is determined and validated experimentally with phantom images and calculation of a B_1 map. Finally, a novel, ''self-compensating'' spin-locking pulse which dramatically reduces these image artifacts is presented, providing a more robust implementation of $T_{1\rho}$ imaging despite spatial variations in B_1.

* Corresponding author. Fax: 1-215-573-2113.
E-mail address: Sridhar@mail.mmrrcc.upenn.edu (S.R. Charagundla).

1090-7807/03/$ - see front matter © 2003 Elsevier Science (USA). All rights reserved.
doi:10.1016/S1090-7807(02)00197-0

2. Theory

2.1. Description of pulse sequence

$T_{1\rho}$ imaging can be performed with a variety of pulse sequences [10,12–16]. We have implemented a three-pulse preparatory pulse cluster pre-appended to a fast spin-echo imaging sequence (Fig. 1), a modification of a sequence used by Mulkern et al. [12,15]. This strategy affords some flexibility in the choice of imaging sequence and the same pulse cluster can be pre-appended to other sequences as desired. It should be noted, however, that the choice of imaging sequence can introduce image contrast that is independent of $T_{1\rho}$ and intrinsic to the imaging sequence. With this in mind, we use centric phase-encoding and the shortest "effective" TE available in the fast spin-echo sequence to minimize T_2 contrast.

The initial hard pulse (labeled P_1) nutates magnetization into the transverse plane, a 90° phase-shifted spin-locking pulse (labeled SL) with amplitude B_{sl} is applied for some time TSL, and a final hard pulse (labeled P_2) is applied, phase-shifted by 180°, to return the $T_{1\rho}$-relaxed magnetization to the longitudinal axis for imaging. B_{sl} is some fraction of the maximum available RF field B_1. Residual transverse magnetization is crushed with a gradient. Ideally, the hard pulses are calibrated to be 90° pulses.

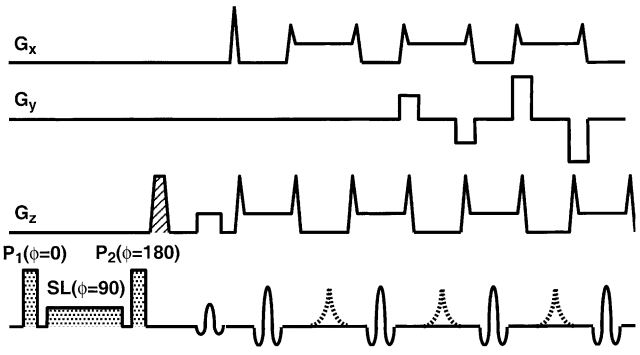

Fig. 1. $T_{1\rho}$-weighted fast spin-echo imaging sequence. A three-pulse preparatory cluster consists of a hard π/2 pulse (P_1) followed by a spin-locking pulse (SL) of phase 90°, duration TSL, and amplitude B_{sl}, and a final hard π/2 pulse (P_2) phase-shifted by 180°. A crusher gradient is then applied to dephase any residual longitudinal magnetization. In the setting of B_1 variation, P_1 and P_2 perform some arbitrary flip angle θ. The phase-encoding gradients (G_y) are applied such that k-space is acquired in a centric fashion to minimize T_2-weighted contrast.

2.2. Simulation of arbitrary flip angle

Using the Bloch equations, we can mathematically model the evolution of magnetization under the pulse sequence described above. Fig. 2 contains rotating frame magnetization vector diagrams accompanying the equations presented below. Suppose we have a sample with a thermal equilibrium magnetization normalized to a value of 1. Then,

$$\boldsymbol{M}_x = 0, \quad \boldsymbol{M}_y = 0, \quad \boldsymbol{M}_z = 1. \tag{1}$$

We apply an rf pulse along the x-axis of width τ and amplitude ω_{1x}, causing a $\theta = \omega_{1x}\tau$ flip (hard pulse P_1 in Fig. 1)

$$\begin{aligned} \boldsymbol{M}_x &= 0, \\ \boldsymbol{M}_y &= \sin\theta, \\ \boldsymbol{M}_z &= \cos\theta. \end{aligned} \tag{2}$$

We then apply a spin-locking pulse along the y-axis of amplitude $\omega_{1y} = \gamma B_{sl}$ for a time TSL. The component of magnetization aligned with the spin-locking vector will decay with a time constant $T_{1\rho}$. Magnetization perpendicular to the spin-locking field also decays, but with a time constant $T_{2\rho}$, which can be estimated as the reciprocal average of T_1 and T_2 [17]. Furthermore, magnetization perpendicular to the spin-locking vector will precess about it with an angular frequency ω_{1y}, resulting in a rotation of $\alpha = \omega_{1y}$ TSL

$$\begin{aligned} \boldsymbol{M}_x &= -\cos\theta\sin\alpha \cdot \mathrm{e}^{-\mathrm{TSL}/T_{2\rho}}, \\ \boldsymbol{M}_y &= \sin\theta \cdot \mathrm{e}^{-\mathrm{TSL}/T_{1\rho}}, \\ \boldsymbol{M}_z &= \cos\theta\cos\alpha \cdot \mathrm{e}^{-\mathrm{TSL}/T_{2\rho}}. \end{aligned} \tag{3}$$

Another rf pulse is applied along the x-axis, phase-shifted by 180°, with identical amplitude ω_{1x} and pulse width τ as before (hard pulse P_2 in Fig. 1), causing a rotation of $-\theta$:

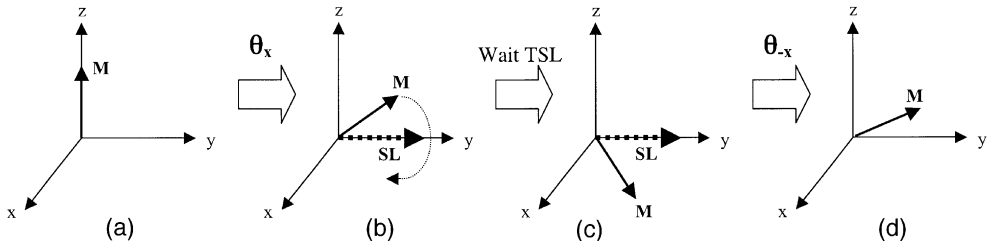

Fig. 2. Magnetization vector diagrams depicting effect of preparatory pulse cluster, as predicted by the Bloch equations. The magnetization is nutated from its equilibrium position (a) by some angle θ after application of the first hard pulse P_1 (b). The spin-locking pulse SL is then applied (b), and the magnetization precesses about the applied rf field by some angle α, resulting in an intermediate orientation (c). The final hard pulse (P_2) nutates the magnetization by $-\theta$, resulting in a complex final orientation (d). The crusher gradient eliminates transverse components.

$$\begin{aligned} \boldsymbol{M}_x &= -\cos\theta\sin\alpha\cdot e^{-TSL/T_{2\rho}},\\ \boldsymbol{M}_y &= \sin\theta\cdot e^{-TSL/T_{1\rho}} - \sin\theta\cos\theta\cos\alpha\cdot e^{-TSL/T_{2\rho}},\\ \boldsymbol{M}_z &= \sin^2\theta\cdot e^{-TSL/T_{1\rho}} + \cos^2\theta\cos\alpha\cdot e^{-TSL/T_{2\rho}}. \end{aligned} \tag{4}$$

This complex magnetization orientation is simplified somewhat with the application of a crusher gradient, which removes transverse magnetization, resulting in

$$\begin{aligned} \boldsymbol{M}_x &= 0,\\ \boldsymbol{M}_y &= 0,\\ \boldsymbol{M}_z &= \sin^2\theta\cdot e^{-TSL/T_{1\rho}} + \cos^2\theta\cos\alpha\cdot e^{-TSL/T_{2\rho}}. \end{aligned} \tag{5}$$

We can relate this to pulse sequence and coil parameters by remembering that $\theta = \gamma B_1 \tau$ and $\alpha = \omega_{1y}$ TSL $= P\gamma B_1$ TSL, where B_1 is the maximum rf amplitude achievable at a given point, τ is the nominal $\pi/2$ pulse width, P is a parameter indicating the spin-lock amplitude expressed as a fraction of the maximum B_1 (i.e., $B_{sl} = P \times B_1$), and TSL is the spin-locking time. The parameter P can be set by the user to achieve the desired spin-locking power.

The remaining longitudinal magnetization in Eq. (5) is then imaged by a fast spin-echo sequence, providing us with a spatial map of its value. Note that if the flip angle θ is calibrated to be a $\pi/2$ pulse, the longitudinal magnetization after the preparatory pulse cluster is simply

$$\boldsymbol{M}_z = e^{-TSL/T_{1\rho}}. \tag{6}$$

For regions where the flip angle is accurately calibrated to be a $\pi/2$ pulse, the longitudinal magnetization contains only information regarding $T_{1\rho}$. However, the more complex expression in Eq. (5) must be used in general, since every coil has some degree of B_1 inhomogeneity. Even if the spin-locking amplitude ω_{1y} is small, it is applied for a comparatively long time, resulting in large rotations (large α). Areas with a large B_1 gradient would exhibit large spatial variation in θ and α, resulting in pronounced artifacts.

2.3. Correction of artifacts with a self-compensating spin-locking pulse

Several strategies exist for reduction of this flip angle dependence. In the preparatory pulse cluster, adiabatic 90° pulses flanking the spin-locking pulse may be implemented instead of hard pulses [18]. Adiabatic pulses provide a robust means of achieving more uniform flip angle despite variations in B_1. However, we use the hard pulses to calibrate rf power; lack of these pulses makes calibration of spin-locking power more problematic. Implementation of shaped adiabatic pulses is also not straightforward. Furthermore, sequences using spin-locking pulses already tend to have relatively high rf power deposition. The inclusion of adiabatic pulses would substantially increase the power deposition of the pulse sequence. Alternatively, Dixon et al. proposed the use of composite pulses to improve the flip-angle profile [19]. We suggest the use of a "rotary echo" spin-locking pulse [17] with a 90° phase shift for half of the spin-locking time and a −90° phase shift for the remainder of the spin-locking time (see Fig. 3). In this case, the magnetization undergoes a rotation of $\alpha/2$ during the first half of the spin-locking pulse, and instead of Eq. (3), we have

$$\begin{aligned} \boldsymbol{M}_x &= -\cos\theta\sin\frac{\alpha}{2}\cdot e^{-TSL/2T_{2\rho}},\\ \boldsymbol{M}_y &= \sin\theta\cdot e^{-TSL/2T_{1\rho}},\\ \boldsymbol{M}_z &= \cos\theta\cos\frac{\alpha}{2}\cdot e^{-TSL/2T_{2\rho}}. \end{aligned} \tag{7}$$

The second half of the spin-locking pulse is applied with a −90° phase, causing a rotation of $-\alpha/2$, and the magnetization becomes

$$\begin{aligned} \boldsymbol{M}_x &= 0,\\ \boldsymbol{M}_y &= \sin\theta\cdot e^{-TSL/T_{1\rho}},\\ \boldsymbol{M}_z &= \cos\theta\cdot e^{-TSL/T_{2\rho}}. \end{aligned} \tag{8}$$

The last θ pulse remains phase-shifted by 180°, resulting in a final magnetization vector of

$$\begin{aligned} \boldsymbol{M}_x &= 0,\\ \boldsymbol{M}_y &= \sin\theta\cos\theta\cdot\left(e^{-TSL/T_{1\rho}} - e^{-TSL/T_{2\rho}}\right),\\ \boldsymbol{M}_z &= \sin^2\theta\cdot e^{-TSL/T_{1\rho}} + \cos^2\theta\cdot e^{-TSL/T_{2\rho}}. \end{aligned} \tag{9}$$

Application of a crusher gradient again destroys transverse magnetization, leaving only $\mathbf{M}_z$. Note, again, that longitudinal magnetization reduces to Eq. (6) if $\theta = \pi/2$. Comparison of Eqs. (5) and (9) reveals that dependence of $\mathbf{M}_z$ on α is removed with use of the self-compensating spin-locking pulse. Despite this, if θ is not $\pi/2$, a portion of magnetization is still lost to $T_{2\rho}$ relaxation, and magnetization undergoing $T_{1\rho}$ relaxation is again degraded by a factor $\sin^2\theta$. This type of spin-locking pulse may be combined with composite excitation pulses for improved performance.

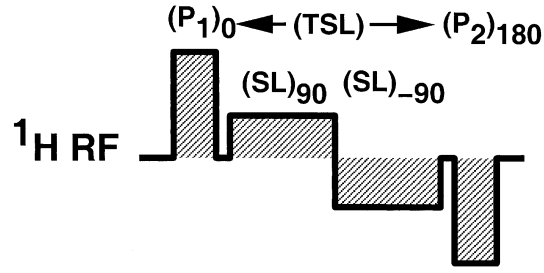

Fig. 3. Modification of preparatory pulse cluster with self-compensating spin-locking pulse. The second half of the spin-locking pulse is phase-shifted by 90° with respect to the first half, correcting for rotations about the applied B_1. The hard pulses P_1 and P_2 remain phase-shifted by 0° and 180°, respectively.

3. Methods

Simulations of theory described above were performed using the Interactive Data Language (IDL, RSI, Boulder, CO) programming environment on a Silicon Graphics workstation (Mountain View, CA). Artificial B_1 maps were generated with linear gradient and Gaussian shapes using dimensionality identical to experimentally obtained images and a range of B_1 values also similar to those obtained experimentally. Artifacts were calculated using Eq. (5) and displayed.

The conventional and self-compensating spin-locking pulse sequences were created by modifying the General Electric (Milwaukee, WI) fast spin-echo pulse sequence, utilizing the EPIC programming language. MR images of a water phantom were obtained on a 4 T whole body GE Signa scanner using a solenoid coil tuned to the ^{1}H Larmor frequency (170 MHz). Imaging was performed using a TR of 2 s, effective TE of 17 ms, field of view of 8 cm, slice thickness of 3 mm, bandwidth of 15 kHz, and acquisition matrix of 256×128.

Initially, calibration of the hard pulses was performed by turning off the spin-locking pulse and P_2 while retaining P_1; the transmit gain (TG) was then titrated until the signal was minimized, implying that P_1 was a $\pi/2$ pulse. TG was fixed at this value.

Images to calculate the B_1 map of the solenoid coil were then obtained. While there are several techniques for calculating the B_1 map of a coil [20–23], we chose to develop an independent approach using our existing pulse sequence. A baseline image was first obtained with both hard pulses (P_1 and P_2) activated; since P_1 and P_2 were 180° apart in phase, they canceled each other out, the crusher gradient had no effect, and the resulting image represented maximum signal intensity (effectively, a flip angle of zero for P_1 and P_2). The P_2 hard pulse was then turned off, and images were acquired with varying amplitudes of P_1. As the amplitude of P_1 approached $\pi/2$, the crusher gradient destroyed more magnetization, and the image signal intensity reduced. That is, for a flip angle θ induced by P_1, image signal intensity followed $\cos(\theta)$. A total of five P_1 amplitudes were utilized, varying from 31 to 92% of the maximum amplitude. The arc-cosine of image signal intensity was plotted as a function of the amplitude of P_1 for each pixel, and the slope of a linear fit yielded a value for B_1 at each pixel.

Hard pulses P_1, P_2, and a standard spin-locking pulse were then activated. The amplitudes of P_1 and P_2 were simultaneously varied to generate artifacts. Images were obtained with a variety of hard pulse amplitudes, spin-locking pulse amplitudes, and spin-locking times. Using the experimentally determined B_1 map, artifacts were simulated using Eq. (5), and the results were compared to the experimentally obtained image artifacts.

Finally, the standard spin-locking pulse was exchanged for a "self-compensating" spin-locking pulse (Fig. 3) for fixed TSL and B_1, and the amplitudes of P_1 and P_2 were again simultaneously varied. Artifacts obtained with the standard spin-locking pulse were compared to those obtained with the "self-compensating" spin-locking pulse. Artifacts were quantified by computing the standard deviation of signal intensity divided by the mean signal intensity (i.e., percent variation) within a central region of interest.

4. Results and discussion

Eq. (5) reveals that, after application of the spin-locking preparatory pulse cluster, the longitudinal magnetization ($\mathbf{M}_z$) has a complex dependence on flip angle, magnetization rotation about the spin-locking vector, and relaxation times. In order to visualize the effects of relaxation times and varying B_1, the value of $\mathbf{M}_z$ as predicted by Eq. (5) was plotted as a function of fraction of maximum B_1 for varying values of $T_{1\rho}$ (Fig. 4) and $T_{2\rho}$ (Fig. 5). In these plots, B_1 (the achievable RF power) is considered to vary from 1 to 100% of a maximum value of 1.25 kHz, with the spin-locking power B_{sl} set equal to B_1 (i.e., $P = 1$) and with flip angles of P_1 and P_2 scaled accordingly. P_1 and P_2 are calibrated to have 90° flip angles when B_1 is at its maximum value of 1.25 kHz. Note that changes in B_1 linearly affect both spin-locking power (B_{sl}) as well as flip angles of the hard pulses P_1 and P_2.

$T_{1\rho}$-weighted images are exquisitely sensitive to flip angle, and are therefore dependent on subtle properties of the B_1 field. In the ideal situation, where the B_1 delivered to the sample is the expected value, P_1 and P_2 represent $\pi/2$ pulses, and artifact-free images can be obtained. However, even with small variations in B_1, P_1 and P_2 become poorly calibrated, and spatial variation in signal intensity is introduced, with an oscillatory dependence on B_1. The amplitude of these oscillations is increased with longer $T_{2\rho}$. The overall signal intensity is increased with longer $T_{1\rho}$. While the absolute amplitude of the oscillations is independent of $T_{1\rho}$, signal decreases with short $T_{1\rho}$, and the significance of these oscillations increases. That is, the amplitude of the oscillations relative to the mean signal intensity increases with short $T_{1\rho}$. Therefore, the significance of image artifacts depends on a variety of experimental parameters, including coil properties and relaxation times of the experimental sample. Indeed, the artifacts vary spatially within an image, and since they exhibit a dependence on spin-locking time and applied spin-locking amplitude (see Eq. (5)), they prevent accurate determination of $T_{1\rho}$ values and $T_{1\rho}$ dispersion. Furthermore, they cannot be corrected by image subtraction or division.

Simulated B_1 maps in the shapes of a Gaussian curve and a linear gradient were mathematically generated, and the expected artifacts arising from such a distribution are

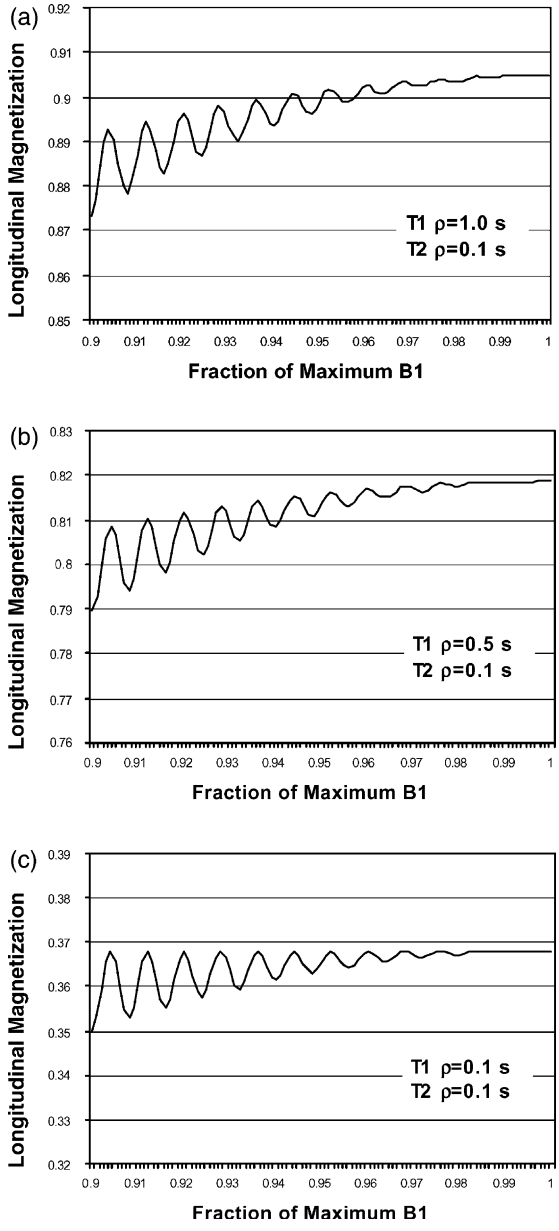

Fig. 4. Theoretically predicted longitudinal magnetization after preparatory pulse cluster as a function of fraction of maximum B_1. B_1 is considered to vary from 1 to 100%, with B_{sl} set equal to B_1 and flip angles of P_1 and P_2 scaling accordingly, such that they are 90° pulses when B_1 is at its maximum value. Note that both B_{sl} and the flip angles of P_1 and P_2 are linearly dependent on the local B_1. Plots (a)–(c) are for varying $T_{1\rho}$ and a fixed $T_{2\rho}$ of 0.1 s; the y-axes are identical in scale but shifted to include the data of interest. $T_{1\rho}$ affects the overall amount of longitudinal magnetization but does not affect the amplitude of oscillations caused by varying B_1; a short $T_{1\rho}$ causes loss of signal.

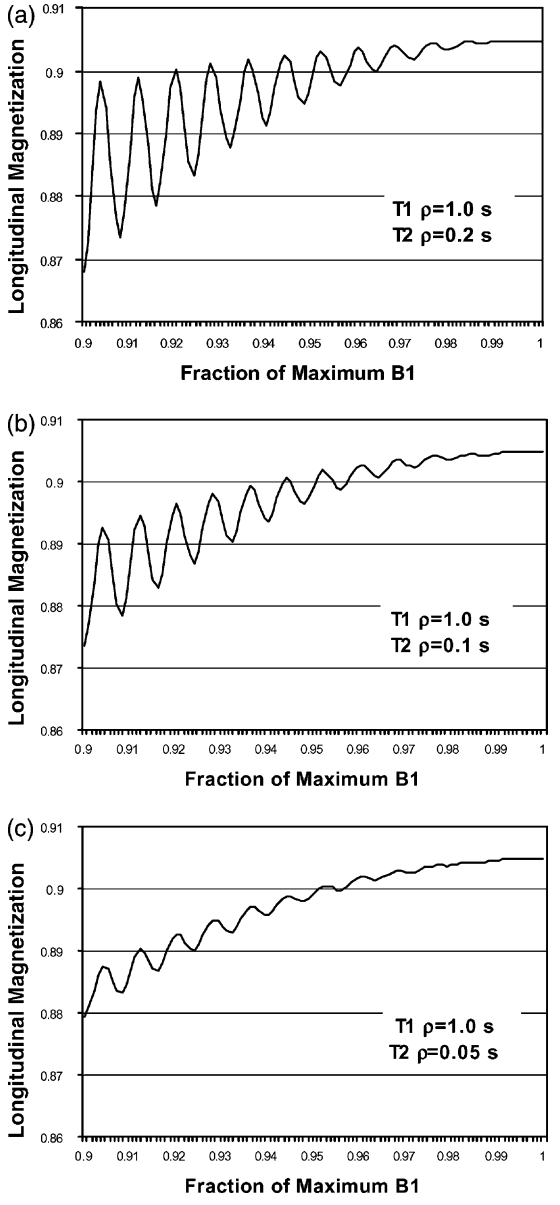

Fig. 5. Theoretically predicted longitudinal magnetization after preparatory pulse cluster as a function of fraction of maximum B_1. B_1 is considered to vary from 1 to 100%, with B_{sl} set equal to B_1 and flip angles of P_1 and P_2 scaling accordingly, such that they are 90° pulses when B_1 is at its maximum value. Note that both B_{sl} and the flip angles of P_1 and P_2 are linearly dependent on the local B_1. Plots (a)–(c) are for varying $T_{2\rho}$ and fixed $T_{1\rho}$ of 1.0 s. $T_{2\rho}$ affects the amplitude of oscillations but not the overall signal intensity; a short $T_{2\rho}$ causes a decrease in the amplitude of oscillations.

shown in Fig. 6. Variations in B_1 are propagated into variations in the image in a highly non-uniform manner, but the overall symmetry of the B_1 profile is preserved. Areas with a larger B_1 gradient exhibit more closely spaced oscillations in image signal intensity.

Image artifacts experimentally obtained for a range of spin-locking times and amplitudes are displayed in Fig. 7; a nominal flip angle of 45° was used. Images are somewhat degraded by motion. The spatial frequency of oscillations increases with increasing spin-locking amplitude or spin-locking time, which is in good agreement with theoretical predictions.

The experimentally determined B_1 map of the solenoid coil is displayed in Fig. 8a. Artifacts theoretically predicted from this B_1 field distribution are displayed in Figs. 8b–d and compared to corresponding experimental images in Figs. 8e–g. Motion artifacts in the source

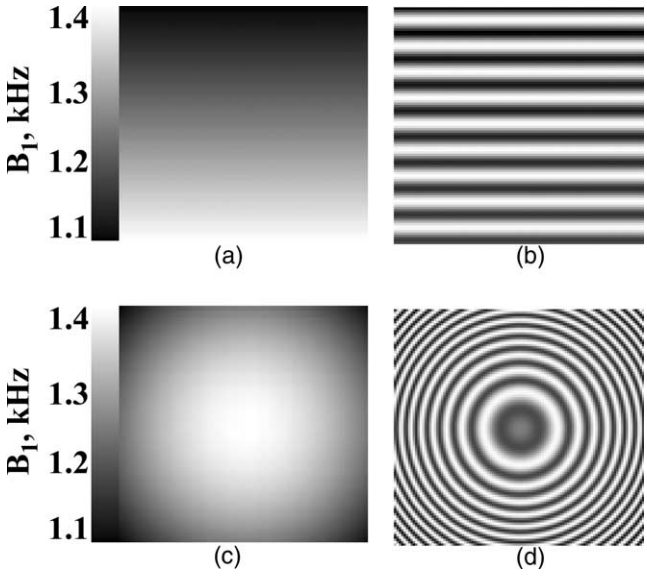

Fig. 6. Simulated B_1 maps and calculated images of corresponding longitudinal magnetization remaining after the spin-locking preparatory pulse cluster. Spin-locking time was set at 200 ms and the nominal flip angle was set at 41°. B_1 is specified in kHz, where the precession frequency around the spin-locking pulse, ν, is equal to γB_1. (a) is a linear B_1 gradient, and (b) is the corresponding simulated image. (c) is a Gaussian B_1 distribution, and (d) is the corresponding simulated image. The symmetry of the B_1 field is preserved in the artifacts generated by the spin-locking sequence.

images used to calculate the B_1 map resulted in small areas of heterogeneity in the B_1 map. This, in turn, translated into distortion of the theoretically predicted artifacts that arise from true B_1 inhomogeneity, seen in Figs. 8b–d. Despite corruption of simulations by motion artifact, comparison of theoretical and experimental images reveals a close similarity, validating the description and explanation of artifacts presented here. Of note, the magnetization-prepared $T_{1\rho}$ imaging sequence conveniently allows acquisition of a B_1 map as well as $T_{1\rho}$-weighted images, with only a few changes in pulse-sequence parameters.

Armed with this understanding of the origin of these artifacts, strategies for their elimination or correction can be discussed. It is possible to remove the artifacts computationally by using Eq. (5), but this requires precise knowledge of B_1, flip angle, and relaxation times $T_{1\rho}$ and $T_{2\rho}$. Needless to say, the purpose of these experiments is often to measure $T_{1\rho}$, so this approach would not be useful. Adiabatic pulses can be used to achieve uniform flip angles despite B_1 inhomogeneity, but this approach increases the degree of RF power deposition, which may place limitations on the amount of spin-locking power available for use. Use of composite pulses for $T_{1\rho}$ imaging has also been described [19]. Given that these image artifacts arise from the α rotation which occurs during the spin-locking pulse, phase-shifting the second half of the spin-locking pulse by 180° with respect to the first half exactly cancels this rotation, and should reduce such artifacts, without requiring knowledge of regional B_1. Images obtained with the conventional spin-locking pulse are compared to those obtained with a self-compensating spin-locking

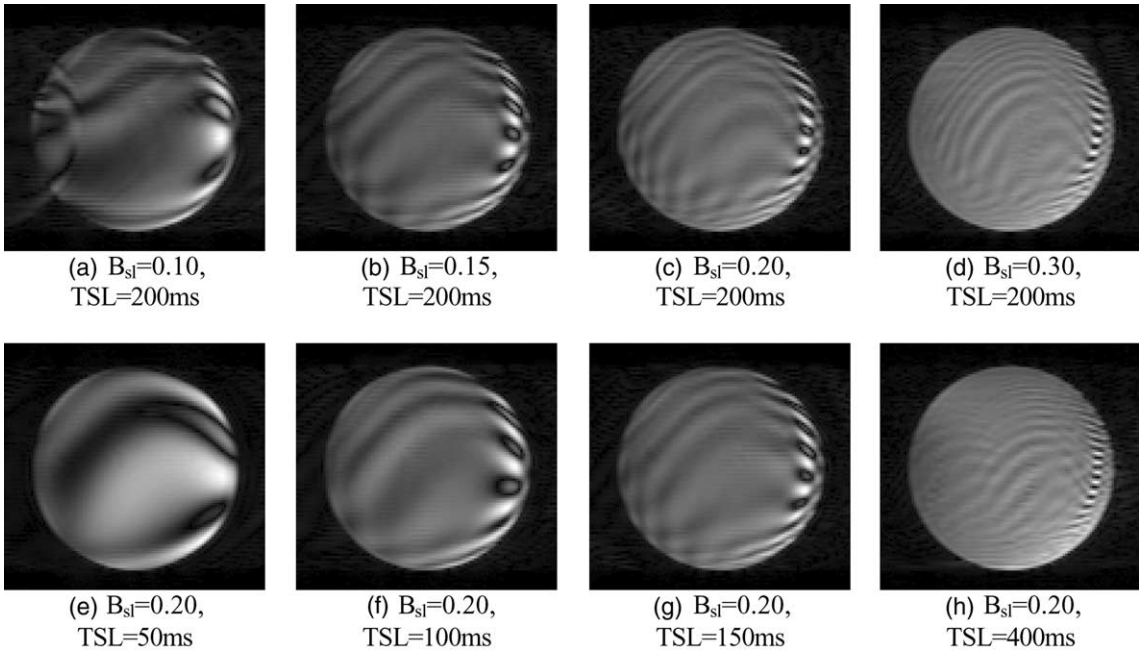

Fig. 7. Artifacts obtained with $T_{1\rho}$-weighted imaging. Flip angles for P_1 and P_2 were set to half of the nominal $\pi/2$ pulse (i.e., 45° flip angle in areas where P_1 and P_2 are well-calibrated). Images in the first row of the table (a)–(d) were acquired with fixed spin-locking time (TSL) and increasing spin-locking amplitude (B_{sl}). Images in the second row (e)–(h) have a fixed spin-locking amplitude and increasing spin-locking time. Parameters for the spin-locking pulse for each image are as listed; B_{sl} is given as a fraction of the maximum B_1, which varied across the coil.

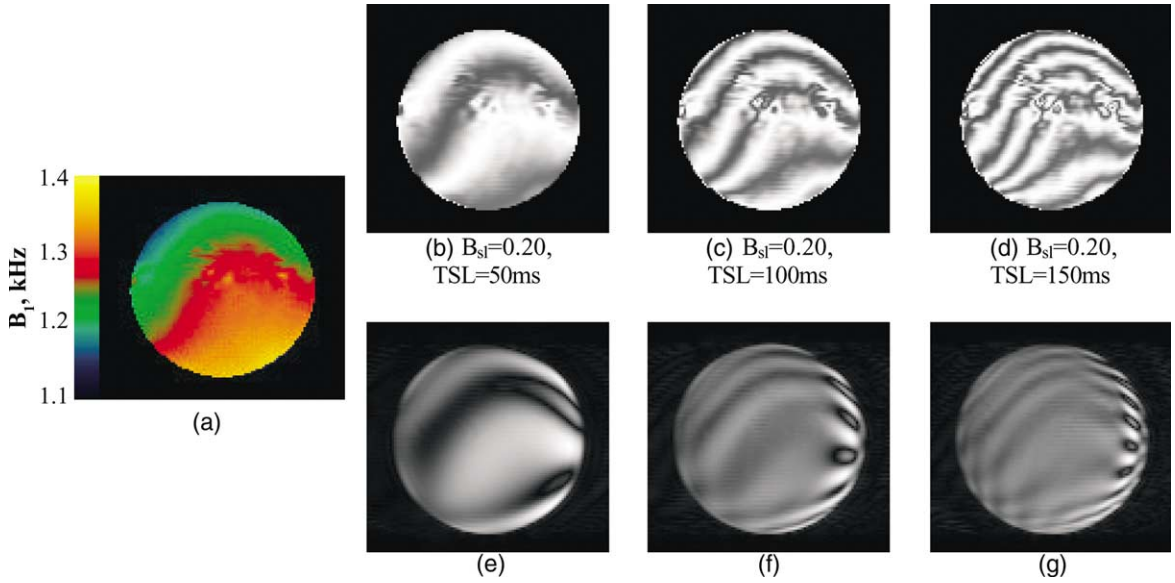

Fig. 8. Experimentally determined B_1 map (a), and comparison of actual and simulated artifacts. B_1 is specified in kHz, were the precession frequency around the spin-locking pulse, ν, is equal to γB_1. Using the measured B_1 map in (a), expected artifacts are calculated using Eq. (5) for given spin-locking parameters and displayed in (b)–(d). Images (e)–(g) represent the corresponding experimentally acquired images. Comparison of experimental and calculated artifacts validates the theory as described.

pulse for a range of flip angles (Fig. 9). For flip angles of 14° and 41°, the corresponding profiles of image signal intensity are provided in Fig. 10. Use of the self-compensating spin-locking pulse results in remarkably consistent images despite large changes in the flip angles P_1 and P_2. This is quantified in Fig. 11, where variation in image signal intensity is plotted as a function of nominal flip angle for images acquired with the conventional and self-compensating spin-locking pulses. The variation in signal intensity is strongly dependent on flip angle when the conventional spin-locking pulse is used. The self-compensating spin-locking pulse dramatically reduces this dependence, resulting in homogeneous images despite a poorly calibrated flip angle.

Use of the self-compensating spin-locking pulse should facilitate quantitative $T_{1\rho}$ imaging despite variations in B_1. However, it should be noted that the second half of the spin-locking pulse will not exactly compensate for the first half if there is significant motion of spins over a gradient of B_1. Also, while the artifacts arising from spatial variation in B_1 are corrected, the varying B_1 affects spin-locking amplitude, which translates into an effect on measured $T_{1\rho}$ times. Therefore, $T_{1\rho}$ values and $T_{1\rho}$ relaxation time maps measured in the presence of an inhomogeneous B_1 field must be interpreted with caution, since spatial variations in $T_{1\rho}$ may actually be due to spatial variations in B_1 rather than properties of the sample itself.

Application of spin-locking pulses in a system with species at a range of chemical shifts or in a system with significant B_0 inhomogeneity can result in more complex rotations arising from off-resonance spin-locking. In the off-resonance rotating frame, the "effective" spin-locking vector is not located in the transverse plane. Therefore, shifting the phase of the spin-locking RF by 180° does not result in an opposite orientation of the

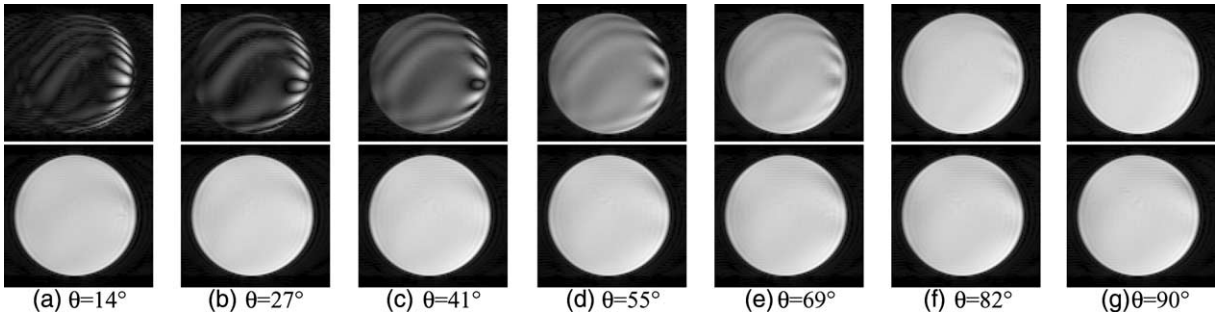

Fig. 9. Reduction in image artifacts through use of self-compensating spin-locking. Images in the top row were obtained with a conventional spin-locking pulse, while images in the bottom row were obtained with a self-compensating spin-locking pulse for a range of flip angles. Images are displayed with equivalent levels and windows. Even severely compromised images are rectified by use of the self-compensating spin-locking pulse. Spin-locking time was 100 ms for all images and B_{sl} was fixed at 20% of the maximum available B_1.

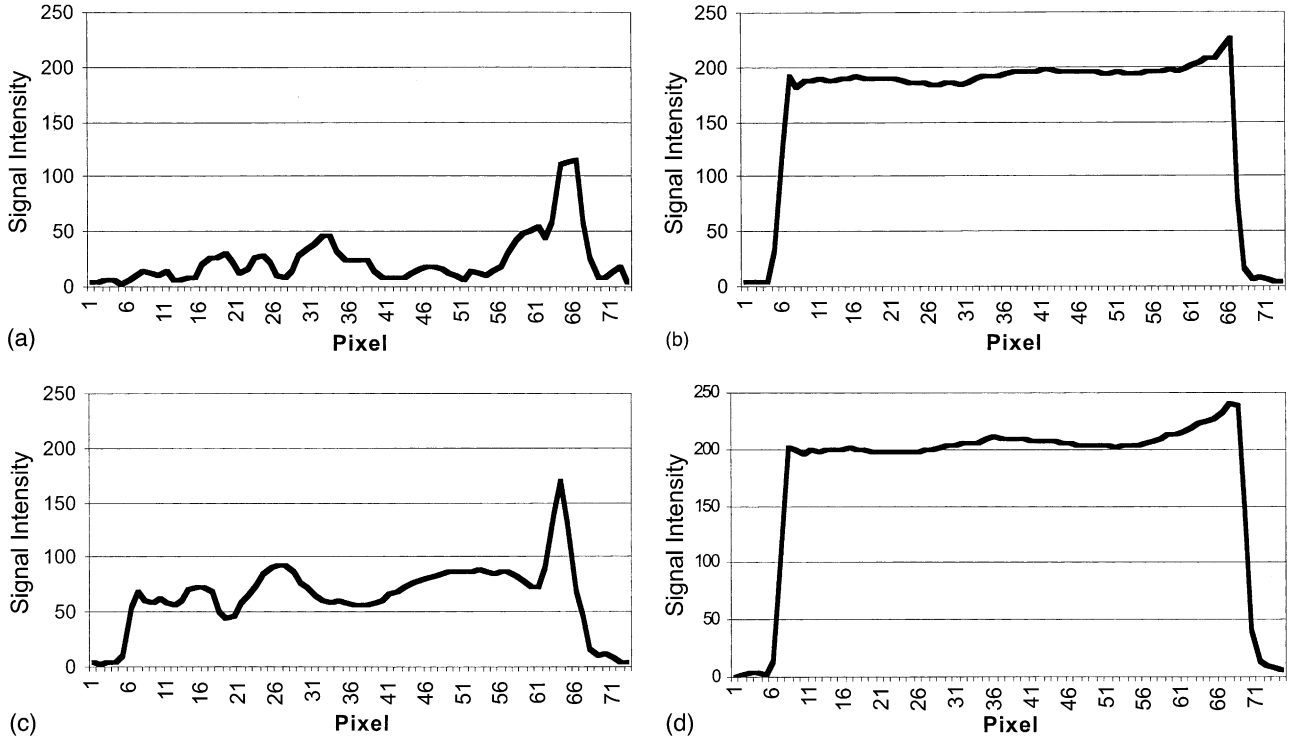

Fig. 10. Signal intensity profiles of images from Figs. 9a and c. Profiles of images obtained with flip angle of 14° using (a) conventional and (b) self-compensating spin-locking pulses, and with flip angle of 41° using (c) conventional and (d) self-compensating spin-locking pulses are displayed. Uniformity of signal intensity across the phantom is markedly improved with use of self-compensating spin-locking.

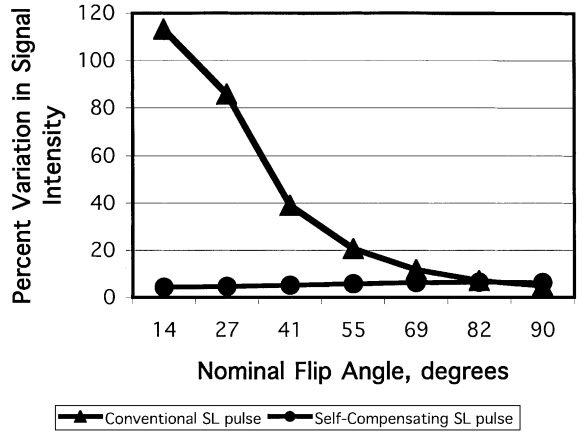

Fig. 11. Comparison of image intensity variation as a function of nominal flip angle for conventional and self-compensating spin-locking. Percent variation in signal intensity is calculated as the standard deviation divided by the mean signal. As demonstrated in Fig. 9, variation in signal intensity with conventional spin-locking increases rapidly for decreasing flip angle. Use of the self-compensating spin-locking pulse results in a more stable image appearance. Baseline variation in signal intensity arises from variations in B_1, particularly at the edges of the coil, and motion artifact.

spin-locking vector. The resultant magnetization rotations and artifacts are not modeled by the theoretical discussion presented here, but the off-resonance effect becomes worse for larger resonance offsets (i.e., greater B_0 inhomogeneity or larger chemical shifts) or weaker spin-locking powers (i.e., lower B_1). Further work is underway to devise a strategy for artifact reduction in this more complex situation.

In these experiments, the self-compensating spin-locking pulse is split into two halves of opposed phase. However, in principle, the pulse can be divided into an arbitrary number of smaller pulses, as long as the positively and negatively phased portions of the pulse are balanced. This draws analogies to the Carr–Purcell–Meiboom–Gill experiment [24,25]. The effects of rapid alternation of spin-locking phase are not known, and are currently under investigation.

$T_{1\rho}$-weighted imaging with a self-compensating spin-locking pulse may allow use of a surface coil, which is perhaps the most dramatic example of B_1 inhomogeneity. Despite large spatial variations in B_1, use of this pulse sequence may generate relatively artifact-free images, facilitating quantitative $T_{1\rho}$ imaging while exploiting the sensitivity and convenience of surface coils. This potential application of the self-compensating spin-locking pulse is also currently under investigation.

In conclusion, a theoretical underpinning for artifacts in $T_{1\rho}$ imaging created by B_1 inhomogeneity has been developed and experimentally validated. A self-compensating spin-locking pulse has been developed which corrects for these artifacts and yields homogeneous images despite large variations in flip angle. With appropriate manipulation of the preparatory pulse cluster, the

same imaging sequence can be utilized for B_1 mapping as well as data acquisition. The sequence has exciting potential application to $T_{1\rho}$ imaging with surface coils.

Acknowledgments

This work was supported by NIH Grants R01-AR45242 and RR-02305.

References

[1] R.R. Rizi, S.R. Charagundla, H.K. Song, R. Reddy, A.H. Stolpen, M.D. Schnall, J.S. Leigh, Proton $T_{1\rho}$-dispersion imaging of rodent brain at 1.9 T, J. Magn. Reson. Imaging 8 (1998) 1090–1096.

[2] U.A. Ramadan, A.T. Markkola, J. Halavaara, J. Tanttu, A.M. Hakkinen, H.J. Aronen, On- and off-resonance spin-lock MR imaging of normal human brain at 0.1 T: possibilities to modify image contrast, Magn. Reson. Imaging 16 (1998) 1191–1199.

[3] H. Poptani, U. Duvvuri, C.G. Miller, A. Mancuso, S. Charagundla, N.W. Fraser, J.D. Glickson, J.S. Leigh, R. Reddy, $T_{1\rho}$ imaging of murine brain tumors at 4 T, Acad. Radiol. 8 (2001) 42–47.

[4] A.T. Markkola, H.J. Aronen, U.A. Ramadan, J.T. Halavaara, J.I. Tanttu, R.E. Sepponen, Determination of $T_{1\rho}$ values for head and neck tissues at 0.1 T: a comparison to T1 and T2 relaxation times, Magn. Reson. Imaging 16 (1998) 377–383.

[5] A.T. Markkola, H.J. Aronen, T. Paavonen, E. Hopsu, L.M. Sipila, J.I. Tanttu, R.E. Sepponen, $T_{1\rho}$ dispersion imaging of head and neck tumors: a comparison to spin lock and magnetization transfer techniques, J. Magn. Reson. Imaging 7 (1997) 873–879.

[6] U. Duvvuri, R. Reddy, S.D. Patel, J.H. Kaufman, J.B. Kneeland, J.S. Leigh, $T_{1\rho}$-relaxation in articular cartilage: effects of enzymatic degradation, Magn. Reson. Med. 38 (1997) 863–867.

[7] S.V. Akella, R. Reddy Regatte, A.J. Gougoutas, A. Borthakur, E.M. Shapiro, J.B. Kneeland, J.S. Leigh, R. Reddy, Proteoglycan induced changes in $T_{1\rho}$-relaxation of articular cartilage at 4 T, Magn. Reson. Med. 46 (2001) 419–423.

[8] A.E. Lamminen, J.I. Tanttu, R.E. Sepponen, H. Pihko, O.A. Korhola, $T_{1\rho}$ dispersion imaging of diseased muscle tissue, Br. J. Radiol. 66 (1993) 783–787.

[9] A. Virta, M. Komu, N. Lundbom, S. Jaaskelainen, H. Kalimo, A. Airio, A. Alanen, M. Kormano, Low field $T_{1\rho}$ imaging of myositis, Magn. Reson. Imaging 16 (1998) 385–391.

[10] R. Reddy, A.H. Stolpen, J.S. Leigh, Detection of ^{17}O by proton $T_{1\rho}$ dispersion imaging, J. Magn. Reson. B 108 (1995) 276–279.

[11] S.R. Charagundla, A.H. Stolpen, J.S. Leigh, R. Reddy, Off-resonance proton $T_{1\rho}$ dispersion imaging of ^{17}O-enriched tissue phantoms, Magn. Reson. Med. 39 (1998) 588–595.

[12] S.R. Charagundla, U. Duvvuri, R. Rizi, H. Poptani, A.H. Stolpen, J.S. Leigh, R. Reddy, in: Proceedings of the International Society of Magnetic Resonance in Medicine, 7th Scientific Meeting, Philadelphia, 1999, p. 2106.

[13] H.J. Aronen, U.A. Ramadan, T.K. Peltonen, A.T. Markkola, J.I. Tanttu, J. Jaaskelainen, A.M. Hakkinen, R. Sepponen, 3D spin-lock imaging of human gliomas, Magn. Reson. Imaging 17 (1999) 1001–1010.

[14] G.E. Santyr, R.M. Henkelman, M.J. Bronskill, Spin locking for magnetic resonance imaging with application to human breast, Magn. Reson. Med. 12 (1989) 25–37.

[15] R.V. Mulkern, S. Patz, M. Brooks, D.C. Metcalf, F.A. Jolesz, Spin-lock techniques and CPMG imaging sequences: a critical appraisal of $T_{1\rho}$ contrast at 0.15 T, Magn. Reson. Imaging 7 (1989) 437–444.

[16] R.E. Sepponen, J.A. Pohjonen, J.T. Sipponen, J.I. Tanttu, A method for $T_{1\rho}$ imaging, J. Comput. Assist. Tomogr. 9 (1985) 1007–1011.

[17] I. Solomon, Rotary spin echoes, Phys. Rev. Lett. 2 (1959) 301–302.

[18] A. Tannus, M. Garwood, Adiabatic pulses, NMR Biomed. 10 (1997) 423–434.

[19] W.T. Dixon, J.N. Oshinski, J.D. Trudeau, B.C. Arnold, R.I. Pettigrew, Myocardial suppression in vivo by spin locking with composite pulses, Magn. Reson. Med. 36 (1996) 90–94.

[20] G.H. Glover, C.E. Hayes, N.J. Pelc, W.A. Edelstein, O.M. Mueller, H.R. Hart, C.J. Hardy, M. O'Donnell, W.D. Barber, Comparison of linear and circular polarization for magnetic resonance imaging, J. Magn. Reson. 64 (1985) 255–270.

[21] J.P. Hornak, J. Szumowski, R.G. Bryant, Magnetic field mapping, Magn. Reson. Med. 6 (1988) 158–163.

[22] E.K. Insko, L. Bolinger, Mapping of the radiofrequency field, J. Magn. Reson. A 103 (1993) 82–85.

[23] G.J. Barker, A. Simmons, S.R. Arridge, P.S. Tofts, A simple method for investigating the effects of non-uniformity of radio-frequency transmission and radiofrequency reception in MRI, Br. J. Radiol. 71 (1998) 59–67.

[24] S. Meiboom, D. Gill, Modified spin-echo method for measuring nuclear relaxation times, Rev. Sci. Instrum. 29 (1958) 688–691.

[25] G.E. Santyr, R.M. Henkelman, M.J. Bronskill, Variation in measured transverse relaxation in tissue resulting from spin locking with the CPMG sequence, J. Magn. Reson. 79 (1988) 28–44.